

BIROn - Birkbeck Institutional Research Online

Pogge von Strandmann, Philip A.E. and Fraser, W. and Hammond, S. and Tarbuck, G. and Wood, I. and Oelkers, E. and Murphy, M. (2019) Experimental determination of Li isotope behaviour during basalt weathering. *Chemical Geology* 517 , pp. 34-43. ISSN 0009-2541.

Downloaded from: <https://eprints.bbk.ac.uk/id/eprint/27380/>

Usage Guidelines:

Please refer to usage guidelines at <https://eprints.bbk.ac.uk/policies.html>
contact lib-eprints@bbk.ac.uk.

or alternatively

Experimental determination of Li isotope behaviour during basalt weathering

Philip A.E. Pogge von Strandmann^{1*}, Wesley T. Fraser², Samantha J. Hammond³, Gary Tarbuck¹, Ian G. Wood¹, Eric H. Oelkers¹, Melissa J. Murphy¹

¹London Geochemistry and Isotope Centre (LOGIC), University College London and Birkbeck, University of London, Gower Place, London, WC1E 6BT.

²Geography, Oxford Brookes University, Oxford, OX3 0BP

³School of Environment, Earth and Ecosystems Sciences, The Open University, Walton Hall, Milton Keynes, MK7 6AA

*Corresponding author: p.strandmann@ucl.ac.uk

Abstract

Silicate weathering is the primary control of atmospheric CO₂ concentrations on multiple timescales. However, tracing this process has proven difficult. Lithium isotopes are a promising tracer of silicate weathering. This study has reacted basalt sand with natural river water for ~9 months in closed experiments, in order to examine the behaviour of Li isotopes during weathering. Aqueous Li concentrations decrease by a factor of ~10 with time, and $\delta^7\text{Li}$ increases by ~19‰, implying that Li is being taken up into secondary phases that prefer ⁶Li. Mass balance using various selective leaches of the exchangeable and secondary mineral fractions suggest that ~12–16% of Li is adsorbed, and the remainder is removed into neoformed secondary minerals. The exchangeable fractionation

factors have a $\Delta^7\text{Li}_{\text{exch-soln}} = -11.6$ to -11.9‰ , while the secondary minerals impose $\Delta^7\text{Li}_{\text{secmin-soln}} = -22.5$ to -23.9‰ . Overall the experiment can be modelled with a Rayleigh fractionation factor of $\alpha = 0.991$, similar to that found for natural basaltic rivers. The mobility of Li relative to the carbon-cycle-critical cations of Ca and Mg changes with time, but rapidly evolves within one month to remarkably similar mobilities amongst these three elements. The evolution shows a linear relationship with $\delta^7\text{Li}$ (largely due to a co-variation between aqueous [Li] and $\delta^7\text{Li}$), suggesting that Li isotopes have the potential to be used as a tracer of Ca and Mg mobility during basaltic weathering, and ultimately CO_2 drawdown.

1.0 Introduction

Chemical weathering of continental silicate rocks is one of the primary drivers of the long-term carbon cycle and climate (Chamberlin, 1899; Walker et al., 1981). Weathering provides nutrients to the ocean to fertilise primary productivity, clay particles to help bury organic carbon (Hawley et al., 2017), and, critically, alkalinity and cations such as Ca and Mg for the precipitation of marine carbonate (Berner et al., 1983). All of these processes sequester atmospheric CO_2 on various timescales, making chemical weathering a fundamental Earth climate system process.

Significant effort has gone into understanding and quantifying silicate weathering, both in the present (e.g. Maher, 2011; West et al., 2005), and in the geological past (e.g. Foster and Vance, 2006; Pogge von Strandmann et al., 2017a; Vance et al., 2009). Traditionally, marine radiogenic strontium isotopes have been used to determine past weathering changes (McArthur et al., 2001), but

51 their interpretation is far from unambiguous, because seawater isotope ratios
52 are impacted by hydrothermal inputs and riverine isotope ratios are strongly
53 dependent on the lithology undergoing weathering. This is further complicated
54 by the inability to distinguish between carbonate and silicate weathering, where
55 only the latter draws down CO₂ on the long-term (Allegre et al., 2010; Oliver et
56 al., 2003). Hence, other tracers have been sought – ideally ones that are relatively
57 unaffected by lithology, by carbonate weathering (which does not affect pCO₂ on
58 >10⁴ year timescales) or by biology and plant growth. So far, the only tracer that
59 meets all these criteria is lithium isotopes.

60 Lithium isotopes (reported as $\delta^7\text{Li}$, the ‰ deviation from a normalising
61 standard) are unaffected by carbonate weathering, because silicates are orders
62 of magnitude more concentrated in Li than carbonates (Kisakürek et al., 2005;
63 Millot et al., 2010; Pogge von Strandmann et al., 2017b), or by plant growth or
64 primary productivity (Lemarchand et al., 2010; Pogge von Strandmann et al.,
65 2016). The $\delta^7\text{Li}$ range in primary silicate rocks (continental crust ~0‰; basalt
66 3–5‰ (Elliott et al., 2006; Sauzeat et al., 2015)) is narrow compared to that
67 observed in rivers draining those rocks ($\delta^7\text{Li}$ = 2–44‰, mean 23‰ (Dellinger et
68 al., 2015; Huh et al., 1998; Pogge von Strandmann et al., 2006)). This range is due
69 to the formation of secondary minerals (clays, zeolites and Fe-Mn-Al
70 oxyhydroxides) during weathering, where these minerals preferentially take up
71 the light isotope, ⁶Li, driving residual river and soil waters isotopically heavy
72 (Vigier et al., 2008; Wimpenny et al., 2010). These secondary minerals also
73 adsorb Li onto their exchangeable sites, imposing the same isotopic fractionation
74 direction (Hindshaw et al., 2019; Pistiner and Henderson, 2003). Hence, Li
75 isotopes in natural waters are controlled by the ratio of primary mineral

dissolution (low $\delta^7\text{Li}$) relative to secondary mineral formation (driving solution $\delta^7\text{Li}$ high). This ratio is known as the “weathering congruency” (Misra and Froelich, 2012; Pogge von Strandmann and Henderson, 2015), which may be used as a tracer of chemical weathering intensity (Dellinger et al., 2015). Overall, this ratio also informs on the efficiency of weathering in removing CO_2 , because if cations are being trapped by secondary minerals on the continents within clays and soils, they will not enter the ocean to form carbonate and sequester CO_2 .

However, while the general mechanics of Li isotope fractionation during weathering are fairly well understood, there is less information available on the precise processes that $\delta^7\text{Li}$ traces, such as whether the primary fractionation mechanism is adsorption onto secondary mineral surfaces, uptake into interlayer sites, or via structural or lattice-bound incorporation into neoformed minerals (Hindshaw et al., 2019; Pistiner and Henderson, 2003; Pogge von Strandmann et al., 2010; Wimpenny et al., 2015). Further, fractionation factors and reaction kinetics are also poorly known.

In this study, we react basalt with river water for around nine months in closed system experiments, following the methods of previous experiments (Jones et al., 2012). The primary goal is to examine Li isotope behaviour during these weathering experiments, to determine which phases affect Li isotopes during weathering, and to quantify their response.

2.0 Methods

2.1 Experimental methods

Following the methods of Jones et al. (2012), approximately 250g of the natural basaltic sand used in the Jones et al. experiments was placed in 1L pre-

leached PTFE beakers containing 900ml of water. This sand was collected from the bottom of the Borgarfjörður estuary in Iceland, and was characterised by Jones et al. (2012). These data are repeated in Supplemental Table 1 for completeness' sake. The sand consists of fairly fresh basalt (for example it contains significant basaltic glass), but also contains small amounts of phyllosilicates only just detectable by X-Ray Diffraction, as described below. For the water to be naturally charge-balanced and have a natural amount of alkalinity, the water used in the experiments was collected from the local Great Ouse River in eastern England. While the composition of this water is not identical to that in Iceland where the sand was sampled, the similarities in temporal fluid concentration behaviour (described below) between this study and Jones et al. (2012), which used Icelandic water, suggest that the differences in these water compositions only has a minor effect on experimental results.

Two identical experiments were run at 20°C in a shaking bath reactor, in order to determine that the Li isotope behaviour was not anomalous. Closed systems were used (rather than through-flow reactors) in order to be able to mass balance the reactants, and to facilitate retrieval of isotopic fractionation factors. Trace element concentrations were only determined from one of the experiments. At periodic intervals, the water pH was measured, and 50 ml of water was removed and filtered through 0.2µm cellulose acetate syringe filters, and stored in pre-cleaned PTFE bottles. Sampling frequency was initially daily, but decreased throughout the experiment (Table 1).

Post-experiment, the reacted basalt was dried and stored. The pre- and post-experimental basalts were also leached, to examine their exchangeable fraction. This leach followed the Tessier method, by leaching the basalt in 1M

sodium acetate for 1 hour at room temperature (Hindshaw et al., 2019; Pogge von Strandmann et al., 2013; Tessier et al., 1979). Following this, the residue was leached for 1 hour with 0.6M HCl, which attacks the secondary mineral fraction, i.e. clays as well as oxyhydroxides and zeolites (Pogge von Strandmann et al., 2014; Tessier et al., 1979). Bulk basalt was dissolved in a standard method of concentrated HF-HNO₃-HClO₄, followed by HNO₃ and 6M HCl.

2.2 XRD and FTIR methods

X-ray powder diffraction analysis was carried out on a “whole sample” basis. Samples were prepared by grinding the material under ethanol using an agate pestle and mortar and the dried powder was side-filled against a ground-glass surface into a rectangular sample holder 20 x 20 mm in area and 1.5 mm deep. Diffraction patterns were collected with Co radiation, using a PANalytical X’Pert Pro diffractometer with Bragg-Brentano parafocusing reflection geometry. This instrument is equipped with a Ge(1 1 1) Johansson-type focusing monochromator, producing a CoK α ₁ incident beam. The X-ray tube was operated at 40 kV and 30 mA. Variable-width divergence and anti-scatter slits were used, together with a 15 mm wide beam mask in the incident beam, so as to illuminate a constant 15mm × 15mm area of the sample; 0.04 radian Soller slits were present in both the incident and diffracted beams to reduce the axial divergences. The X-ray detector was an “X’Celerator” position-sensitive detector; this device covers an angular range in 2 θ of $\pm 1.061^\circ$, with an effective fixed step size of 0.0167° . Data were collected over the 2 θ range from 5° to 70° ($20.5 \text{ \AA} < d < 1.56 \text{ \AA}$), with data collection times of 15 hours.

150 Fourier-transform infrared (FTIR) analyses were conducted on dried
151 samples using a Perkin-Elmer Spectrum2 (Seer Green, Buckinghamshire, UK)
152 attenuated total reflectance-FTIR (ATR-FTIR) spectrometer, fitted with a single-
153 bounce diamond ATR cell. A total of 8 scans were used to generate an average
154 spectrum for each sample at a resolution of 4cm^{-1} . Spectra spanned the range
155 $4000\text{-}600\text{ cm}^{-1}$. All samples were analysed in triplicate.

156 Clay minerals typically show a pronounced broad absorption band
157 centred at $c.3300\text{cm}^{-1}$ associated with hydroxyl (OH) groups interacting via
158 hydrogen bonding within the clay structure, thus an increase in OH spectral
159 response indicates an increase in clay mineral content of a sample.

160

161 *2.3 Concentration analyses*

162 The solution concentrations were analysed at The Open University, using
163 an Agilent 8800 triple quadrupole inductively coupled plasma mass
164 spectrometer (ICP-QQQ-MS). The instrument has two quadrupole mass filters,
165 which are separated by a collision / reaction cell (allowing targeted interference
166 removal in the cell). We ran in two modes of analysis, no gas for Li (as no
167 interference ions are present on mass) and in He collision mode for all other
168 analytes. In no gas mode, oxide levels (measured as CeO^+/Ce^+) were at 0.96%
169 and doubly charged species ($\text{Ce}^{2+}/\text{Ce}^+$) at 1.80%. In He mode, these were at
170 0.44% and 1.30% respectively.

171 Prior to analysis, samples were diluted 10 fold from the original solution
172 in 2% HNO_3 to allow analysis of all masses in the same analytical session.

173 Analyses were calibrated against a suite of synthetic multi-element solutions,
174 which were made up to cover the range of concentrations in the experimental

solutions. An on-line internal standard (Rh and In) was added to each sample and standard also, to monitor and correct for instrument drift. In addition, drift was further monitored by running a measurement block consisting of the original water used in the experiments, one of the calibration standards and a 2% HNO₃ blank every 5 – 6 unknowns (5 times during the analytical session). Where concentrations are above the detection limit in the initial water, reproducibility is better than 2.5% (relative standard deviation from the mean of the five measurements). Accuracy was also determined using the international river water reference standard SLRS-5, and was within uncertainty of certified values. Lithium and silicon are not certified in SLRS-5, so in this case we compared to published concentrations and were also within uncertainty (Heimbürger et al., 2013).

Major elemental concentrations of the starting basalt are taken from Jones et al. (2012), except for Li concentrations, which were determined by ICP-MS analyses in a similar manner to the dissolved concentrations, while running BCR-2 as an external standard, whose values were within uncertainty ($\pm 6\%$) of isotope-dilution determined Li concentrations in BCR-2 (Pogge von Strandmann et al., 2011). All concentrations are reported in the Supplement.

The elemental ratios of the leachates were determined using a Varian 720ES ICP-OES. Samples were calibrated using matrix-matched synthetic standards (i.e. in Na acetate and dilute HCl).

2.4 Li isotope analyses

Approximately 15ml of water was evaporated, and passed through a two-stage cation exchange column procedure, using AG50W X-12 resin, and eluting with dilute HCl (Pogge von Strandmann et al., 2011). Column splits were collected before and after the main elute, and analysed for Li content, to determine how much Li was in the sample. Using this method, it was determined that >99.9% of sample was collected in the main column elution. Purified samples were analysed using a new Nu Plasma 3 multi-collector ICP-MS at the LOGIC laboratories. A sample-standard bracketing procedure was used relative to the IRMM-016 standard. Each sample was measured three separate times during an analytical procedure, repeat measurements being separated by several hours, but during the same analysis session. Each individual measurement consisted of 10 ratios (50 s total integration time), giving a total integration time of 150 s/sample for the three repeat measurements that constitute a single analysis (n=1). We use the 2sd (standard deviation) of these three measurements as an assessment of our individual uncertainty, although values reported in Table 1 have also been compounded for the difference in normalising standards described below.

This mass spectrometer has new cones (compared to previous Nu MC-ICP-MSs), and, using the specific “super-lithium cones”, and a Cetac Aridus 2 desolvation system, a 5 µg/L solution gives a signal intensity of 100–140 pA (10–14V) of $^7\text{Li}^+$ at an uptake rate of ~100 µl/min. Background, instrumental Li intensities, typically ~0.07 pA (7mV), were subtracted from the sample and standard intensities. Total procedural blanks were generally indistinguishable from background, and contain <0.003 ng Li.

223 Lithium isotope ratios are commonly reported relative to the LSVEC
 224 standard (Flesch et al., 1973). LSVEC analysed relative to IRMM-016 yields $\delta^7\text{Li} =$
 225 -0.003 ± 0.054 (2se, n=19), which is in close agreement with past corresponding
 226 measurements (Jeffcoate et al., 2004; Phan et al., 2016). All reported $\delta^7\text{Li}$ values
 227 have been re-normalised to LSVEC, and the reported uncertainty has been
 228 propagated to encompass analytical uncertainty on both samples, normalising
 229 standards and LSVEC.

230 Given that this is the first Li isotope study published at the new LOGIC isotope
 231 mass spectroscopy facilities, we have gone to some effort to determine the
 232 accuracy and precision of our analyses. We have therefore analysed seawater
 233 (both IAPSO and North Atlantic seawater) and the USGS rock standards BCR-2
 234 (basalt), G-2 (granite), PCC-1 (peridotite) and SGR-1b (shale). Relative to LSVEC,
 235 seawater $\delta^7\text{Li} = 31.11 \pm 0.38\text{‰}$ (2sd; n=12) (identical to other published values,
 236 e.g. Dellinger et al., 2015; James and Palmer, 2000; Jeffcoate et al., 2004; Pogge
 237 von Strandmann and Henderson, 2015). Our other values also compared well to
 238 published values: BCR-2: $\delta^7\text{Li} = 2.64 \pm 0.31\text{‰}$ (n=5) (e.g. $2.6 \pm 0.3\text{‰}$ (Pogge von
 239 Strandmann et al., 2011); $2.7 \pm 1.3\text{‰}$ (Liu et al., 2013); $2.9 \pm 0.3\text{‰}$ (John et al.,
 240 2012)); G-2: $\delta^7\text{Li} = 0.14 \pm 0.16\text{‰}$ (n=3) (e.g. $0.1 \pm 0.8\text{‰}$ (Phan et al., 2016); $0.6 \pm$
 241 1.8‰ (Sauzeat et al., 2015)); PCC-1: $\delta^7\text{Li} = 8.72 \pm 0.13\text{‰}$ (n=3) (e.g. $8.9 \pm 0.4\text{‰}$
 242 (Magna et al., 2006)); SGR-1b: $\delta^7\text{Li} = 4.00 \pm 0.24\text{‰}$ (e.g. $4.7 \pm 0.7\text{‰}$ (Phan et al.,
 243 2016); $3.6 \pm 0.4\text{‰}$ (Pogge von Strandmann et al., 2017b); $4.9 \pm 1.9\text{‰}$ (Hindshaw
 244 et al., 2018)). Hence, our standard results show that our Li isotope analyses are
 245 accurate, and have a long-term external precision (for the twelve months the
 246 new laboratory has been operational) of better than $\pm 0.4\text{‰}$ (2sd).

247

248 3.0 Results

249 *3.1 Concentrations*

250 The same basalt sand as used by Jones et al. (2012) was also used for this
251 experiment, and details are given in Supplementary Table 1. The Li
252 concentration of the unreacted basalt is 5.53 $\mu\text{g/g}$, similar to MORB and other
253 Icelandic basalts (Elliott et al., 2006; Pistiner and Henderson, 2003). The post-
254 reaction basalts have indistinguishable bulk Li concentrations of 5.3–5.6 $\mu\text{g/g}$.

255 Compared to the bulk basalt composition, the sodium acetate leach
256 (exchangeable fraction) of the unreacted basalt has considerably higher Mg/Si
257 ratios (mass ratio $\text{Mg/Si}_{\text{bulk basalt}} = 0.27$, while $\text{Mg/Si}_{\text{exch}} = 25.3$) (Table 2). Silicon
258 (as a neutral species) should not be present in the exchangeable leach, and its
259 presence (albeit at very low concentrations) implies that the leach is not fully
260 efficient due to a small contribution of Si from the dissolution of silicate minerals
261 (Hindshaw et al., 2019). Lower Mg/K ratios in the exchangeable fractions
262 ($\text{Mg/K}_{\text{bulk basalt}} = 13.7$, while $\text{Mg/K}_{\text{exch}} = 0.75$), and undetectable Al and Fe
263 demonstrate that the exchangeable fraction of the initial basalt is enriched in the
264 elements that would be expected to partition into this fraction (Renforth et al.,
265 2015; Sigfusson et al., 2008; Tessier et al., 1979). The exchangeable fractions of
266 the reacted basalts have somewhat lower Mg/Si (8.2–9.5). Li/Si is also several
267 orders of magnitude higher in the unreacted exchangeable fraction than the
268 initial bulk basalt (0.04 compared to 3×10^{-5}), and decreases slightly in the
269 reacted basalts (0.015–0.03), showing that Li is considerably more affiliated with
270 sorption than Si.

In contrast, the HCl leach (that should attack the secondary mineral phases) of the unreacted basalt has similar Mg/Si to the bulk basalt (0.29 compared to 0.27). However, elements that would be expected to be enriched in clays and oxyhydroxides are enriched: Al/Si is 0.63 in the leach, compared to 0.36 in the bulk basalt, while Fe/Si is 0.92 compared to 0.53. Li/Si is also over an order of magnitude higher in the leaches. The reacted basalts' leached Li/Si ratios are slightly lower than the unreacted basalt (Table 2). Overall, the leaches appear to have targeted the expected phases: the adsorbed fraction is enriched in exchangeable cations, and the secondary mineral plus Fe and Al oxyhydroxides fraction is enriched in elements such as Fe, Al and Li, as demonstrated before for basalts (Chapela Lara et al., 2017; Hindshaw et al., 2019; Opfergelt et al., 2014; Pogge von Strandmann et al., 2012; Pogge von Strandmann et al., 2014; Sigfusson et al., 2008; Tessier et al., 1979).

The concentrations of the initial unreacted water, and the experimental aqueous solutions are given in Table 1. A sample of the initial water was kept at the same conditions as the experiments (without any contact with basalt, and with atmospheric contact) to examine how the pH evolved. The initial pH of this aqueous solution started at 7.1, increased to 7.6 after a month, and then decreased to 7.3 by the end of the experiment (Table 1). Both basalt-water experiments showed the same pattern, but were consistently about 0.2 pH units lower.

Aqueous solution concentration behaviour is generally similar to that reported by Jones et al. (2012). Most major elemental concentrations increase with reaction time (Fig. 1), with an overall 3% increase in Na, 24% in Mg, 93% in Si, while at the same time K and Ca concentrations decrease slightly (on the

order of 10%). This behaviour for the individual elements is similar to that observed by Jones et al. (2012), although the enrichment amounts vary. This is likely due to the different composition of the waters used in these experiments (Jones et al., 2012). Minor elements like Al and Mn also increase. Almost all of these elements reach apparent steady-state (stable concentrations) after ~50–100 days after the beginning of the experiments. Importantly for these experiments, as also shown by Jones et al. (2012), Li concentrations decrease, from 13.5 $\mu\text{g/L}$ in pre-experimental water to 1.3 $\mu\text{g/L}$ by the end of the experiment. By comparison, the flow-weighted mean global river concentration is 1.5 $\mu\text{g/L}$ (Huh et al., 1998). This behaviour results in a rapid increase in some elemental ratios including Mg/Na, which attains a near steady value after ~12 days. The Li/Na ratios evolve to a constant value more slowly, due to the more gradual decline in Li concentrations.

3.2 Li isotopes

The $\delta^7\text{Li}$ of the pre-experimental bulk basalt is 4.4‰, similar to other Icelandic and MORB basalts (Elliott et al., 2006; Pogge von Strandmann et al., 2006; Pogge von Strandmann et al., 2012; Vigier et al., 2009). The post-experimental bulk basalts from the two experiments have a $\delta^7\text{Li}$ of 4.1–4.5‰, within analytical uncertainty of the pre-experimental basalt (Table 2).

The exchangeable fraction (sodium acetate leach) of the pre-experimental basalt has a $\delta^7\text{Li}$ of 17.8‰, with a Li concentration of 0.7 $\mu\text{g/L}$ (compared to a total procedural blank of 0.03 $\mu\text{g/L}$). Given the presence of minor quantities of Si in these leaches from the dissolution of silicate minerals (see Section 3.1), the leachate $\delta^7\text{Li}$ is likely slightly lower value than if the leach were fully efficient.

The secondary mineral fraction (HCl leach) has a $\delta^7\text{Li}$ of 5.3‰ with a Li concentration in the leach of 11.6 ng/g. As for the exchangeable leach, the secondary mineral leach is unlikely to have been totally efficient (Hindshaw et al., 2019), although elemental ratios in this leach (Table 2) are close to stoichiometry for some examples of smectite.

The post-experiment exchangeable fractions have $\delta^7\text{Li}$ values of 21.3 and 21.8‰, while the HCl leach has $\delta^7\text{Li}$ values of 9.3–10.8‰ (i.e. 4.0–5.5‰ higher than that of the unreacted pre-experimental basalt leach). Concentrations must be normalised to the amount of material in the experiment to be meaningful. Thus, exchangeable Li increases from 1.1 μg in the total (250g) pre-experiment basalt to 2.5–2.9 μg post-experiment. Similarly, the HCl leach increases from 17.6 μg to 27–27.5 μg .

The $\delta^7\text{Li}$ of the initial reactive aqueous fluid is 14‰, and these fluids then exhibit an increase with time to a final value of 33.3‰ in both experiments (Fig. 2). The simultaneous decrease in Li concentrations of these fluids results in a negative correlation between $\delta^7\text{Li}$ and [Li], which is frequently observed in basaltic rivers (Pogge von Strandmann et al., 2010; Pogge von Strandmann et al., 2006; Vigier et al., 2009), although natural rivers tend to have slightly lower concentrations (Fig. 3), likely due to the relatively higher [Li] in the starting solution of these experiments. In both experiments, an approximate steady-state appears to have been reached, with both Li concentrations and isotopes approximately stable for the last 125 days of the experiment.

4.0 Discussion

4.1 Lithium mass balance

The mass balance of lithium in the experiments can be used to determine the destination of Li lost from the fluid. In principle there are two phases that could be taking up Li from the fluid: the exchangeable fraction (i.e. sorbed Li) and the secondary mineral fraction (i.e. Li substituting into the crystal structures of neoforming minerals)(Chan and Hein, 2007; Millot and Girard, 2007; Pistiner and Henderson, 2003; Vigier et al., 2008; Wimpenny et al., 2015; Wimpenny et al., 2010). For this mass balance, we assume that the Na acetate leach represents the exchangeable fraction, while the subsequent HCl leach represents Li recovered from secondary minerals (including oxyhydroxides and clays or zeolites).

We also assume that Li added to solution by primary basalt dissolution can be calculated by assuming that the increase in fluid of Mg or Si represents stoichiometric dissolution (Jones et al., 2012), such that the Li/Mg or Li/Si concentration ratios remain constant during dissolution. Stoichiometric weathering is unlikely to be a perfect assumption, given that both Mg and Si are also known to partition into secondary minerals as well (e.g. (Opfergelt et al., 2014; Pogge von Strandmann et al., 2012)). However, constant elemental ratios during dissolution is likely a robust assumption, as Li is a moderately incompatible element, and does not partition preferentially into any primary basaltic minerals (Penniston-Dorland et al., 2017). In any case, the amount of Li added from basalt dissolution is minor compared to that lost from solution. According to the Mg and Si concentration increase, between 0.015 and 0.07 g of the ~250 g basalt samples dissolved during the experiments, which is around 4% of the total Li mass balance (~0.4µg Li, assuming constant Li/Mg ratios).

In the experiments, when normalised to the amount of material used, the exchangeable fraction gained $\sim 1.4\text{--}1.8\mu\text{g Li}$, while the secondary minerals gained $\sim 9.4\text{--}9.9\mu\text{g Li}$. The solution (when corrected for fluid loss due to sampling) lost $\sim 11.4\mu\text{g Li}$ by the end of the experiment.

Given weighing errors and propagated analytical uncertainty, the experiments therefore can be mass balanced, with around $\sim 82\text{--}87\%$ of the Li lost from the fluid substituting into secondary phases, and $\sim 12\text{--}16\%$ being taken into the exchangeable fraction (Fig. 4). This result demonstrates that the sorbed fraction is of sufficient importance to be an integral consideration of future lithium weathering studies.

4.2 Mineral saturation states

Mineral saturation states in the fluids were calculated using the PHREEQC programme (Parkhurst and Appelo, 1999). Basaltic primary minerals (olivine, plagioclase, pyroxene) are undersaturated in all the experimental fluids, and hence are likely to dissolve. The undersaturation of these minerals is maintained by supersaturation (and hence likelihood of precipitation) of secondary minerals (Gíslason et al., 1996). For example, both kaolinite and smectite are consistently supersaturated in all the experimental solutions. However, while kaolinite's saturation is broadly constant, that of smectite increases with time. Iron oxyhydroxides (e.g. amorphous $\text{Fe}(\text{OH})_3$, another common basaltic secondary mineral) starts out undersaturated, but becomes supersaturated after about 4 days of reaction.

Mineral saturation states provide insight into whether neoformation or sorption is dominantly controlling Li isotope fractionation. There is a clear co-

variation between the saturation state of smectite (Aberdeen-montmorillonite) and $\delta^7\text{Li}$ that does not exist for any other modelled secondary minerals. As the smectite saturation state increases, so as the likelihood of precipitation increases, the $\delta^7\text{Li}$ also increases, because more ^6Li is being incorporated into precipitating smectites. It is also noticeable that extrapolation of the trend line ($r^2 = 0.94$) back into undersaturated conditions ($\text{SI} < 0$) leads to the initial $\delta^7\text{Li}$ values of the basalts used (Fig. 5). In other words, when no smectite is forming, it appears that the solutions would have an identical $\delta^7\text{Li}$ value to primary basalt (i.e. congruent weathering). As smectite precipitation increases, ^6Li is preferentially removed from the fluid, increasing solution $\delta^7\text{Li}$ values. In contrast, were Fe oxyhydroxide the dominant secondary mineral controlling Li, its undersaturated conditions at the start of the experiment should result in unfractionated Li isotopes, which is not observed.

Therefore, this confirms that clay formation strongly affects Li isotope fractionation (Bouchez et al., 2013; Wimpenny et al., 2015; Wimpenny et al., 2010), but also adds to the mass balance argument made above, that it is secondary mineral formation, rather than sorption, that is largely controlling Li isotope fractionation in this experiment (84–88% of Li by mass balance) (Hindshaw et al., 2019; Pistiner and Henderson, 2003; Vigier et al., 2008; Wimpenny et al., 2015).

4.3 Li isotope fractionation

Assuming that the Li concentrations and isotope ratios measured in the exchangeable and secondary mineral fractions represent fractionation from the

youngest (most recent) experimental fluids in the dissolved fraction, it is possible to calculate fractionation factors into both solid fractions.

The $\Delta^7\text{Li}_{\text{exch-soln}}$ of the experiments is -11.6 to -11.9‰, while the $\Delta^7\text{Li}_{\text{secmin-soln}}$ is -22.5 to -23.9‰. The weighted fractionation factor of total Li taken into both fractions combined is on average $\sim -22\text{‰}$. Iceland basaltic rivers exhibit $\Delta^7\text{Li}$ values between unleached suspended loads and complementary dissolved loads of up to $\sim -36\text{‰}$, although with an average of -22‰ , similar to the results here (Pogge von Strandmann et al., 2006; Vigier et al., 2009). Rivers from the basaltic Azores exhibit an average $\Delta^7\text{Li}_{\text{susp-soln}} \sim -17 \pm 7\text{‰}$ (Pogge von Strandmann et al., 2010), while rivers draining the Columbia River Basalts show an average $\Delta^7\text{Li}_{\text{susp-soln}} \sim -17 \pm 4\text{‰}$ (Liu et al., 2015). Comparatively, alteration of the fresh oceanic basalts (one of the primary sinks of Li from seawater) cause $-26 \pm 1\text{‰}$ fractionation from solution (in this case seawater), while weathered oceanic basalts exhibit $-22 \pm 4\text{‰}$ (Chan et al., 1992), and dredged ophiolite is fractionated by $\sim -17\text{‰}$ (Coogan et al., 2017). Even subaerial basalts, when weathered by seawater, show -21‰ fractionation (Pogge von Strandmann et al., 2008). Thus, while there are apparently subtle differences in fractionation between different terrains (bearing in mind that riverine suspended loads do not necessarily only consist of secondary minerals), observed fractionations appears to be broadly similar, around $\sim 20\text{‰}$. The observed fractionation in these experiments is also similar to the overall variability observed in a global compilation of published riverine values (Murphy et al., 2019), and the mean discharge-weighted $\delta^7\text{Li}$ of $\sim 23\text{‰}$ observed in rivers (Huh et al., 1998).

In several different river studies, including in basaltic terrains, Li/Na ratios have been reported to have a similar behaviour as Li isotope ratios,

because Na is considered to be highly mobile (and hence remains in the fluid phase) (Dellinger et al., 2015; Liu et al., 2015; Millot et al., 2010; Pogge von Strandmann et al., 2017b). Hence, Li/Na ratios are likely also be controlled by the ratio of dissolution to precipitation, and might be a good proxy for the extent of water-rock interaction time.

The relationship between $\delta^7\text{Li}$ and Li/Na has been possible to simulate with isotopic fractionation models, which yield the fractionation factors that might be mineral-specific (Pogge von Strandmann et al., 2017b). Hence, overall, as Li/Na decreases (because Li is removed from solution relative to Na), $\delta^7\text{Li}$ increases. Generally it seems that most large global rivers can be simulated assuming an equilibrium fractionation relationship, although global basaltic rivers appear to be following more of a Rayleigh fractionation relationship (Pogge von Strandmann et al., 2017b).

In the case of this study, the data show a logarithmic relationship between Li/Na and $\delta^7\text{Li}$ as it evolves from the starting point of the initial water (Fig. 6). This relationship can be modelled with a Rayleigh fractionation equation, given that the experiments in this study behaved as a closed system. Hence, ~90% of the initial Li was taken up into various secondary phases. All the data form a single fractionation relationship stemming from the initial fluid composition, with a best-fit Rayleigh α value of 0.991 ($r^2 = 0.96$). This is generally similar to fractionation factors reported during natural basalt weathering: MORB-seawater and basalt particle-seawater interaction have $\alpha \sim 0.985$ (Chan et al., 1992; Pogge von Strandmann et al., 2008), and the best-fit to a global compilation of basaltic rivers is to a Rayleigh relationship with $\alpha \sim 0.992$ (Pogge von Strandmann et al., 2017b). This factor is likely related both to the experimental fluid composition

(and hence the starting fluid composition and the composition of the basalt)
because it is likely to control the precise secondary mineralogy.

4.4 Mobility and $\delta^7\text{Li}$

One of the prevailing questions about the use of Li isotopes as a palaeo-weathering proxy is what process precisely these isotopes are tracing. Generally Li isotopes are considered to be able to trace weathering congruency (Pogge von Strandmann and Henderson, 2015) or weathering intensity (Dellinger et al., 2015), but not directly weathering rates (Pogge von Strandmann et al., 2017b). Often in models of palaeo-records, Li isotopes are considered likely to be able to act as a tracer for the riverine Li concentration and/or flux (Lechler et al., 2015; Li and West, 2014; Pogge von Strandmann et al., 2017a; Pogge von Strandmann et al., 2013). However, even if $\delta^7\text{Li}$ were a perfect tracer for the Li flux, there is little knowledge of how these fluxes might relate to those of elements critical to the precipitation of marine carbonate and hence to the carbon cycle, such as Ca or Mg. Hence, it has become important to determine the relationship between the behaviour of Li in relation to that of Ca and Mg.

Elemental mobility during weathering is the tendency of a particular element to go into the fluid phase versus being taken up by secondary minerals during weathering. During basaltic weathering, Na is the most mobile major cation (Gíslason et al., 1996), and hence the mobility of other cations is commonly reported as the relative mobility to Na, where the formula is $(x/\text{Na})_{\text{solution}}/(x/\text{Na})_{\text{rock}}$. In Icelandic basalts relatively mobile elements such as Ca and Mg are approximately $\sim 10\times$ less mobile than Na, while immobile elements such as Al or Fe are about three orders of magnitude less mobile than

Na (Gíslason et al., 1996). Natural studies have rarely measured Li concentrations, and hence the relative difference between the weathering mobility of Li and Ca or Mg remains poorly understood.

In the case of our experiments, the final equilibrium mobilities are similar to the natural values reported by Gíslason et al. (1996), but show a clear trend of evolution with time. Magnesium starts at around 13× less mobile than Na, but within 4 days has evolved slightly to its final value of ~11× less mobile (Fig. 7). Cations such as Ca behave similarly, albeit in the case of Ca the relative mobility decreases slightly with time. The relative mobility of lithium, on the other hand, changes more dramatically, starting out at almost 75% of the mobility of Na, and decreasing, and stabilising at, about 10% after ~100 days reaction. Over 80% of this change in mobility occurs within the first month of the experiment. This observation supports the hypothesis that secondary mineral formation, rather than solely the more rapidly reacting exchangeable fraction, is largely affecting the Li isotope composition. Exchangeable reactions take a few hours to occur (Pistiner and Henderson, 2003), while the kinetics of secondary mineral formation are thought to be relatively slow (on the order of 10^{-19} mol/cm²/s (Yokoyama and Banfield, 2002)). However, those observations on secondary mineral kinetics were largely made using major elements, not more sensitive trace elements such as Li, and our data suggest that at least amorphous secondary phases begin to form within a few days.

From the point of using Li as a tracer of overall chemical weathering processes, especially the transport of Ca and Mg to the oceans to form carbonate thereby drawing down CO₂, the relative mobility difference between Li and Ca or Mg is more revealing: Li starts the experiment as ~15× more mobile than Ca

(and $\sim 9\times$ more mobile than Mg), but these values decrease with time during the experiment to Li being only $2.2\times$ more mobile than Ca (and $1.0\times$ as mobile as Mg)(Fig. 8). This temporal evolution is almost entirely driven by the significant changes in Li concentration, although there is also a relatively small decrease in Ca mobility as well. Most of these change occurs within the first month of the experiments, while for the subsequent >7 months significantly less changes occur. The relatively slower evolution of Li mobility (compared to major elements) suggests that Li may be a very sensitive element for tracing very early and small amounts of incipient secondary mineral formation. Certainly measurements using X-Ray Diffraction (XRD) of the pre- and post-experiment basalts cannot distinguish the amounts of phyllosilicates or Fe oxides in the two basalts. Hence the partitioning of Li is clearly more sensitive to the inception of secondary mineral formation than XRD.

Equally, no discernible difference in clay-associated OH abundance could be detected between the starting samples and the experimental samples using Fourier-transform infrared (FTIR). This therefore also suggests that the difference between pre- and post-experiment samples are small.

These results therefore suggest two points: 1) the changes in the phases controlling the Li isotope ratios are very small, showing that $\delta^7\text{Li}$ is considerably more sensitive to these changes than the more standard methods of XRD and FTIR; 2) once a steady-state is reached, Li has a similar mobility to both Ca and Mg, meaning that Li is a useful tracer for the behaviour during weathering of these two critical elements (Pogge von Strandmann et al., 2016).

Notably, given that only Li isotope ratios are useful in the marine geological record, and not absolute Li concentrations, there is a correlation

544 between solution $\delta^7\text{Li}$ and the relative mobility of Li to Ca and Li to Mg (Fig. 8). In
545 the case of Ca, the negative relationship has an r^2 of 0.99. After four days of
546 reaction, the Li to Ca mobility begins to decrease and $\delta^7\text{Li}$ to further increase
547 (Fig. 8), again largely driven by the change in Li concentration correlating with
548 $\delta^7\text{Li}$. In other words, during the experiment, the Li/Ca and Li/Mg ratios of the
549 secondary minerals must be increasing as Li is increasingly removed from
550 solution. After a month (34 days) of reaction, the rates of change of Li to Ca
551 mobility and of $\delta^7\text{Li}$ dramatically decline, as the reaction reaches apparent
552 steady-state.

553 Thus, not only does Li rapidly (from a natural weathering perspective)
554 reach a similar mobility to Ca and Mg, but also $\delta^7\text{Li}$ is therefore an excellent
555 tracer of Li mobility. This is useful from the point of palaeo-reconstructions. For
556 example, speleothem reconstructions using Li isotopes have determined the Li
557 mobility over time (Pogge von Strandmann et al., 2017c). The same calculations
558 can be performed for seawater archives, assuming that both hydrothermal input
559 rates (possibly via reconstructed spreading rates), and the starting rock
560 composition of rivers are “known”. Using the equilibrium Li to Ca mobility
561 (based on $\delta^7\text{Li}$) for the riverine input, it would then be possible to determine the
562 past behaviour of riverine Ca or Mg fluxes from Li isotopes. Before this can be
563 properly adopted, similar experiments are required on different primary
564 lithologies (e.g. granites, shales, etc.), but it raises the possibility of $\delta^7\text{Li}$ being a
565 direct quantitative proxy for the behaviour of Ca and Mg, and hence CO_2
566 drawdown over geologic time.

567

5.0 Conclusions

Basalts were experimentally reacted with water in closed reactors for over nine months. During this time, while solution major elements such as Mg or Si increased in concentration in the fluid phase (implying basalt dissolution), dissolved Li concentrations decreased, and $\delta^7\text{Li}$ increased, implying removal of Li into or sorption onto secondary phases.

Mass balance calculations using selective leaches of the pre- and post-experiment basalts, shows that, of the Li removed from solution, ~12–16% was taken up by the exchangeable fraction (imparting a ~12‰ fractionation to $\delta^7\text{Li}$), and the remainder by neoformed secondary minerals (imparting ~23‰ fractionation). For at least the final 6 months of the experiment, Li fractionation appears to have reached steady-state conditions, and isotope ratios remain approximately constant. The $\delta^7\text{Li}$ vs. Li/Na trends of the experiment follow an overall closed-system Rayleigh relationship with an $\alpha = 0.991$, similar to other basaltic rivers.

The solution Li isotope ratio also correlates with the modelled saturation index of smectite, where an extrapolation of the trend to saturated conditions (SI = 0) converges towards basaltic $\delta^7\text{Li}$ compositions, further implying that neoformation of secondary minerals may be largely controlling solution $\delta^7\text{Li}$. This suggests that Li isotopes are more susceptible to this early mineral formation than major element ratios, or to standard methods of clay detection such as X-Ray diffraction and Fourier-transform infrared. Equally, this implies that the onset of clay formation (or even amorphous clays) is much more rapid than initially thought (on the order of a few days to months).

Finally, the relatively mobility of Li to those cations critical in the carbon cycle (Ca and Mg) evolves with time, but rapidly (within one month) reaches a point where the behaviour of Li is broadly similarly mobile to both elements. There is also a direct correlation between $\delta^7\text{Li}$ and this mobility, implying that Li isotopes can be used to trace Li mobility, and therefore can be used to trace Ca and Mg mobility (at least during basalt weathering), and ultimately CO_2 drawdown.

Acknowledgements

The experiments and experimental equipment were funded by Royal Society Research Grant 537708. PPvS and MJM were funded by ERC Consolidator grant 682760 CONTROLPASTCO₂. We thank Ed Tipper, Josh Wimpenny and an anonymous reviewer for their comments.

- Allegre, C.J. et al., 2010. The fundamental role of island arc weathering in the oceanic Sr isotope budget. *Earth and Planetary Science Letters*, 292(1-2): 51-56.
- Berner, R.A., Lasaga, A.C., Garrels, R.M., 1983. The Carbonate-Silicate Geochemical Cycle and Its Effect on Atmospheric Carbon-Dioxide over the Past 100 Million Years. *American Journal of Science*, 283(7): 641-683.
- Bouchez, J., von Blanckenburg, F., Schuessler, J.A., 2013. Modeling novel stable isotope ratios in the weathering zone. *American Journal of Science*, 313.
- Chamberlin, T.C., 1899. An attempt to frame a working hypothesis of the cause of glacial periods on an atmospheric basis. *Journal of Geology*, 7(6): 545-584.
- Chan, L.H., Edmond, J.M., Thompson, G., Gillis, K., 1992. Lithium isotopic composition of submarine basalts: implications for the lithium cycle in the oceans. *Earth and Planetary Science Letters*, 108(1-3): 151-160.
- Chan, L.H., Hein, J.R., 2007. Lithium contents and isotopic compositions of ferromanganese deposits from the global ocean. *Deep-Sea Research*, 54: 1147-1162.
- Chapela Lara, M., Buss, H.L., Pogge von Strandmann, P.A.E., Schuessler, J.A., Moore, O.W., 2017. The influence of critical zone processes on the Mg

626 isotope budget in a tropical, highly weathered andesitic catchment.
 627 *Geochimica Et Cosmochimica Acta*, 202: 77–100.
 628 Coogan, L.A., Gillis, K.M., Pope, M., Spence, J., 2017. The role of low-temperature
 629 (off-axis) alteration of the oceanic crust in the global Li-cycle: Insights
 630 from the Troodos ophiolite. *Geochimica Et Cosmochimica Acta*, 203: 201–
 631 215.
 632 Dellinger, M. et al., 2015. Riverine Li isotope fractionation in the Amazon River
 633 basin controlled by the weathering regimes. *Geochimica Et Cosmochimica*
 634 *Acta*, 164: 71–93.
 635 Elliott, T., Thomas, A., Jeffcoate, A., Niu, Y.L., 2006. Lithium isotope evidence for
 636 subduction-enriched mantle in the source of mid-ocean-ridge basalts.
 637 *Nature*, 443(7111): 565–568.
 638 Flesch, G.D., Anderson, A.R., Svec, H.J., 1973. A secondary isotopic standard for
 639 $6\text{Li}/7\text{Li}$ determinations. *Int. J. Mass Spectrom. Ion Process.*, 12: 265–272.
 640 Foster, G.L., Vance, D., 2006. Negligible glacial-interglacial variation in
 641 continental chemical weathering rates. *Nature*, 444(7121): 918–921.
 642 Gíslason, S.R., Arnorsson, S., Armannsson, H., 1996. Chemical weathering of
 643 basalt in southwest Iceland: Effects of runoff, age of rocks and
 644 vegetative/glacial cover. *American Journal of Science*, 296(8): 837–907.
 645 Hawley, S.M., Pogge von Strandmann, P.A.E., Burton, K.W., Williams, H.M.,
 646 Gíslason, S.R., 2017. Continental weathering and terrestrial
 647 (oxyhydr)oxide export: Comparing glacial and non-glacial catchments in
 648 Iceland. *Chemical Geology*, 462: 55–66.
 649 Heimbürger, A. et al., 2013. SLRS-5 Elemental Concentrations of Thirty-Three
 650 Uncertified Elements Deduced from SLRS-5/SLRS-4 Ratios. *Geostandards*
 651 *and Geoanalytical Research*, 37(1): 77–85.
 652 Hindshaw, R.S., Aciego, S.M., Tipper, E.T., 2018. Li and U Isotopes as a Potential
 653 Tool for Monitoring Active Layer Deepening in Permafrost Dominated
 654 Catchments. *Frontiers in Earth Science*, 6.
 655 Hindshaw, R.S. et al., 2019. Experimental constraints on Li isotope fractionation
 656 during clay formation. *Geochimica Et Cosmochimica Acta*, 250: 219–237.
 657 Huh, Y., Chan, L.H., Zhang, L., Edmond, J.M., 1998. Lithium and its isotopes in
 658 major world rivers: Implications for weathering and the oceanic budget.
 659 *Geochimica Et Cosmochimica Acta*, 62(12): 2039–2051.
 660 James, R.H., Palmer, M.R., 2000. The lithium isotope composition of international
 661 rock standards. *Chemical Geology*, 166(3-4): 319–326.
 662 Jeffcoate, A.B., Elliott, T., Thomas, A., Bouman, C., 2004. Precise, small sample size
 663 determinations of lithium isotopic compositions of geological reference
 664 materials and modern seawater by MC-ICP-MS. *Geostandards and*
 665 *Geoanalytical Research*, 28(1): 161–172.
 666 John, T. et al., 2012. Volcanic arcs fed by rapid pulsed fluid flow through
 667 subducting slabs *Nature Geoscience*, 5: 489–492.
 668 Jones, M.T., Pearce, C.R., Oelkers, E.H., 2012. An experimental study of the
 669 interaction of basaltic riverine particulate material and seawater.
 670 *Geochimica Et Cosmochimica Acta*, 77: 108–120.
 671 Kisakürek, B., James, R.H., Harris, N.B.W., 2005. Li and $\delta^7\text{Li}$ in Himalayan rivers:
 672 Proxies for silicate weathering? *Earth and Planetary Science Letters*,
 673 237(3-4): 387–401.

674 Lechler, M., Pogge von Strandmann, P.A.E., Jenkyns, H.C., Prosser, G., Parente, M.,
 675 2015. Lithium-isotope evidence for enhanced silicate weathering during
 676 OAE 1a (Early Aptian Selli event). *Earth and Planetary Science Letters*,
 677 432: 210–222.

678 Lemarchand, E., Chabaux, F., Vigier, N., Millot, R., Pierret, M.C., 2010. Lithium
 679 isotope systematics in a forested granitic catchment (Strengbach, Vosges
 680 Mountains, France). *Geochimica Et Cosmochimica Acta*, 74: 4612–4628.

681 Li, G., West, A.J., 2014. Evolution of Cenozoic seawater lithium isotopes: Coupling
 682 of global denudation regime and shifting seawater sinks. *Earth and*
 683 *Planetary Science Letters*, 401: 284–293.

684 Liu, X.-L., Rudnick, R.L., McDonough, W.F., Cummings, M.L., 2013. Influence of
 685 chemical weathering on the composition of the continental crust: Insights
 686 from Li and Nd isotopes in bauxite profiles developed on Columbia River
 687 Basalts. *Geochimica Et Cosmochimica Acta*, 115: 73–91.

688 Liu, X.-M., Wanner, C., Rudnick, R.L., McDonough, W.F., 2015. Processes
 689 controlling $\delta^7\text{Li}$ in rivers illuminated by study of streams and
 690 groundwaters draining basalts. *Earth and Planetary Science Letters*, 409:
 691 212–224.

692 Magna, T., Wiechert, U., Halliday, A.N., 2006. New constraints on the lithium
 693 isotope compositions of the Moon and terrestrial planets. *Earth and*
 694 *Planetary Science Letters*, 243(3–4): 336–353.

695 Maher, K., 2011. The role of fluid residence time and topographic scales in
 696 determining chemical fluxes from landscapes. *Earth and Planetary*
 697 *Science Letters*, 312: 48–58.

698 McArthur, J.M., Howarth, R.J., Bailey, T.R., 2001. Strontium isotope stratigraphy:
 699 LOWESS version 3: Best fit to the marine Sr-isotope curve for 0–509 Ma
 700 and accompanying look-up table for deriving numerical age. *Journal of*
 701 *Geology*, 109(2): 155–170.

702 Millot, R., Girard, J.P., 2007. Lithium Isotope Fractionation during adsorption
 703 onto mineral surfaces, International meeting, Clays in natural &
 704 engineered barriers for radioactive waste confinement, Lille, France.

705 Millot, R., Vigier, N., Gaillardet, J., 2010. Behaviour of lithium and its isotopes
 706 during weathering in the Mackenzie Basin, Canada. *Geochimica Et*
 707 *Cosmochimica Acta*, 74: 3897–3912.

708 Misra, S., Froelich, P.N., 2012. Lithium Isotope History of Cenozoic Seawater:
 709 Changes in Silicate Weathering and Reverse Weathering. *Science*, 335:
 710 818–823.

711 Murphy, M.J. et al., 2019. Tracing silicate weathering processes in the
 712 permafrost-dominated Lena River watershed using lithium isotopes.
 713 *Geochimica Et Cosmochimica Acta*, 245: 154–171.

714 Oliver, L. et al., 2003. Silicate weathering rates decoupled from the $^{87}\text{Sr}/^{86}\text{Sr}$ ratio
 715 of the dissolved load during Himalayan erosion. *Chemical Geology*, 201(1–
 716 2): 119–139.

717 Opfergelt, S. et al., 2014. Magnesium retention on the soil exchange complex
 718 controlling Mg isotope variations in soils, soil solutions and vegetation in
 719 volcanic soils, Iceland. *Geochimica Et Cosmochimica Acta*, 125: 110–130.

720 Parkhurst, D.L., Appelo, C.A.J., 1999. User's guide to PHREEQC (version 2) - a
 721 computer program for speciation, batch-reaction, one-dimensional
 722 transport, and inverse geochemical calculations.

723 Penniston-Dorland, S., Liu, X.-M., Rudnick, R.L., 2017. Lithium Isotope
 724 Geochemistry, *Rev. Min. Geochem.*, pp. 165–217.
 725 Phan, T.T. et al., 2016. Factors controlling Li concentration and isotopic
 726 composition in formation waters and host rocks of Marcellus Shale,
 727 Appalachian Basin. *Chemical Geology*, 420: 162–179.
 728 Pistiner, J.S., Henderson, G.M., 2003. Lithium-isotope fractionation during
 729 continental weathering processes. *Earth and Planetary Science Letters*,
 730 214(1-2): 327–339.
 731 Pogge von Strandmann, P.A.E., Burton, K.W., James, R.H., van Calsteren, P.,
 732 Gislason, S.R., 2010. Assessing the role of climate on uranium and lithium
 733 isotope behaviour in rivers draining a basaltic terrain. *Chemical Geology*,
 734 270: 227–239.
 735 Pogge von Strandmann, P.A.E. et al., 2006. Riverine behaviour of uranium and
 736 lithium isotopes in an actively glaciated basaltic terrain. *Earth and*
 737 *Planetary Science Letters*, 251: 134–147.
 738 Pogge von Strandmann, P.A.E. et al., 2016. The effect of hydrothermal spring
 739 weathering processes and primary productivity on lithium isotopes: Lake
 740 Myvatn, Iceland. *Chemical Geology*, 445: 4–13.
 741 Pogge von Strandmann, P.A.E. et al., 2017a. Global climate stabilisation by
 742 chemical weathering during the Hirnantian glaciation. *Geochemical*
 743 *Perspective Letters*, 3: 230–237.
 744 Pogge von Strandmann, P.A.E. et al., 2011. Variations of Li and Mg isotope ratios
 745 in bulk chondrites and mantle xenoliths. *Geochimica Et Cosmochimica*
 746 *Acta*, 75: 5247–5268.
 747 Pogge von Strandmann, P.A.E., Frings, P.J., Murphy, M.J., 2017b. Lithium isotope
 748 behaviour during weathering in the Ganges Alluvial Plain. *Geochimica Et*
 749 *Cosmochimica Acta*, 198: 17–31.
 750 Pogge von Strandmann, P.A.E., Henderson, G.M., 2015. The Li isotope response to
 751 mountain uplift. *Geology*, 43(1): 67–70.
 752 Pogge von Strandmann, P.A.E., James, R.H., van Calsteren, P., Gíslason, S.R.,
 753 Burton, K.W., 2008. Lithium, magnesium and uranium isotope behaviour
 754 in the estuarine environment of basaltic islands. *Earth and Planetary*
 755 *Science Letters*, 274(3-4): 462–471.
 756 Pogge von Strandmann, P.A.E., Jenkyns, H.C., Woodfine, R.G., 2013. Lithium
 757 isotope evidence for enhanced weathering during Oceanic Anoxic Event 2.
 758 *Nature Geoscience*, 6: 668–672.
 759 Pogge von Strandmann, P.A.E. et al., 2012. Lithium, magnesium and silicon
 760 isotope behaviour accompanying weathering in a basaltic soil and pore
 761 water profile in Iceland. *Earth and Planetary Science Letters*, 339–340:
 762 11–23.
 763 Pogge von Strandmann, P.A.E. et al., 2014. Chemical weathering processes in the
 764 Great Artesian Basin: Evidence from lithium and silicon isotopes. *Earth*
 765 *and Planetary Science Letters*, 406: 24–36.
 766 Pogge von Strandmann, P.A.E. et al., 2017c. Lithium isotopes in speleothems:
 767 Temperature-controlled variation in silicate weathering during glacial
 768 cycles. *Earth and Planetary Science Letters*, 469: 64–74.
 769 Renforth, P., Pogge von Strandmann, P.A.E., Henderson, G.M., 2015. The
 770 dissolution of olivine added to soil: Implications for enhanced weathering.
 771 *Applied Geochemistry*, 61: 109–118.

- Sauzeat, L., Rudnick, R.L., Chauvel, C., Garcon, M., Tang, M., 2015. New perspectives on the Li isotopic composition of the upper continental crust and its weathering signature. *Earth and Planetary Science Letters*, 428: 181–192.
- Sigfusson, B., Gislason, S.R., Paton, G.I., 2008. Pedogenesis and weathering rates of a Histic Andosol in Iceland: Field and experimental soil solution study. *Geoderma*, 144(3-4): 572-592.
- Tessier, A., Campbell, P.G.C., Bisson, M., 1979. Sequential Extraction Procedure for the Speciation of Particulate Trace Metals. *Analytical Chemistry*, 51(7): 844-851.
- Vance, D., Teagle, D.A.H., Foster, G.L., 2009. Variable Quaternary chemical weathering fluxes and imbalances in marine geochemical budgets. *Nature*, 458: 493–496.
- Vigier, N. et al., 2008. Quantifying Li isotope fractionation during smectite formation and implications for the Li cycle. *Geochimica Et Cosmochimica Acta*, 72: 780–792.
- Vigier, N., Gislason, S.R., Burton, K.W., Millot, R., Mokadem, F., 2009. The relationship between riverine lithium isotope composition and silicate weathering rates in Iceland. *Earth and Planetary Science Letters*, 287(3-4): 434–441.
- Walker, J.C.G., Hays, P.B., Kasting, J.F., 1981. A Negative Feedback Mechanism for the Long-Term Stabilization of Earths Surface-Temperature. *Journal of Geophysical Research-Oceans and Atmospheres*, 86(NC10): 9776-9782.
- West, A.J., Galy, A., Bickle, M., 2005. Tectonic and climatic controls on silicate weathering. *Earth and Planetary Science Letters*, 235(1-2): 211–228.
- Wimpenny, J. et al., 2015. Lithium isotope fractionation during uptake by gibbsite. *Geochimica Et Cosmochimica Acta*, 168: 133–150.
- Wimpenny, J. et al., 2010. The behaviour of Li and Mg isotopes during primary phase dissolution and secondary mineral formation in basalt. *Geochimica Et Cosmochimica Acta*, 74: 5259-5279.
- Yokoyama, T., Banfield, J.F., 2002. Direct determinations of the rates of rhyolite dissolution and clay formation over 52,000 years and comparison with laboratory measurements. *Geochimica Et Cosmochimica Acta*, 66: 2665–2681.

Sample	Time	pH	Na	Mg	Al	Si	K	Ca	Li	$\delta^7\text{Li}$	2sd
	days		mg/L	mg/L	$\mu\text{g/L}$	mg/L	mg/L	mg/L	$\mu\text{g/L}$	‰	
Initial water	0	6.84	48.5	7.87	b.d.l.	2.59	11.1	11.8	13.5	14.7	0.4
15.1	1	6.91	47.8	9.28	8.50	3.19	9.63	11.9	9.9	15.8	0.1
15.2	2	6.86	48.4	9.92	5.58	3.41	9.32	11.5	9.9	16.8	0.5
15.3	4	6.89	48.4	10.6	8.65	3.61	8.95	11.0	8.2	19.6	0.2
15.4	12	7.17	48.6	10.9	11.7	4.22	8.67	10.8	4.7	26.2	0.3
15.5	34	7.60	48.8	11.2	10.7	4.83	8.56	10.6	2.9	31.0	0.2
15.6	68	7.33	48.9	11.2	10.7	5.20	8.46	10.6	2.2	32.7	0.4
15.7	126	7.08	48.7	11.4	12.3	5.71	8.35	10.8	1.6	34.4	0.3
15.8	252	7.04	49.4	11.5	11.7	6.18	8.35	10.8	1.3	33.3	0.3
16.1	1	7.26							9.5	15.4	0.3
16.2	2	7.05							9.5	16.0	0.5
16.3	4	7.13							8.0	19.6	0.6
16.4	12	7.43							4.8	24.1	0.4
16.5	34	7.49							2.8	31.5	0.1
16.6	68	7.29							2.3	33.2	0.1
16.7	126	7.16							1.4	34.9	0.4
16.8	252	7.31							1.4	33.3	0.4

Table 1. Concentration and isotope ratios from the experimental fluids.

812

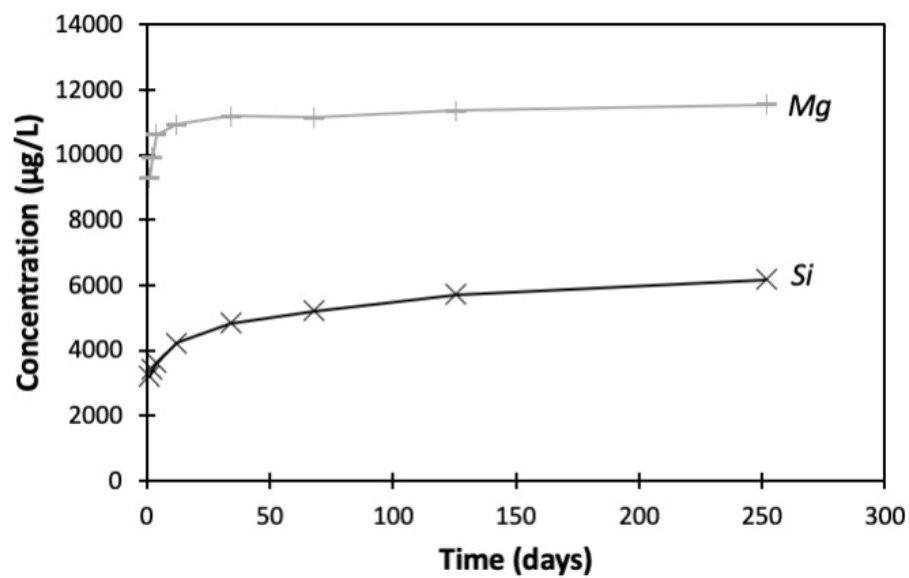
813

Sample	$\delta^7\text{Li}$	2sd	Li in	Mg/Si	Ca/Si	K/Si	Li/Si	Al/Si	Fe
	‰		experiment μg						
Exp 15	21.3	0.4	2.47	9.47	113	12.6	0.030		
Exp 16	21.8	0.5	2.90	8.24	96.4	10.4	0.015		
Unreacted	17.8	0.1	1.10	25.3	104	9.3	0.038		
Exp 15	9.3	0.6	27.5	0.271	0.439	0.014	0.0003	0.567	0.8
Exp 16	10.8	0.1	27.0	0.292	0.426	0.013	0.0002	0.634	0.9
Unreacted	5.3	0.5	17.6	0.294	0.426	0.013	0.0005	0.635	0.9
Exp 15	4.5	0.2	1320						
Exp 16	4.1	0.3	1390						
Unreacted	4.4	0.2	1380	0.269	0.590	0.020	0.00003	0.358	0.5

Table 2. Li amounts and isotope ratios, as well as elemental ratios, from the different

leached and bulk phases. Sec. mins. stands for secondary minerals.

814



815

816 Figure 1. Measured aqueous Mg and Si concentrations during the experiment.

817 Analytical uncertainty is smaller than the symbol sizes.

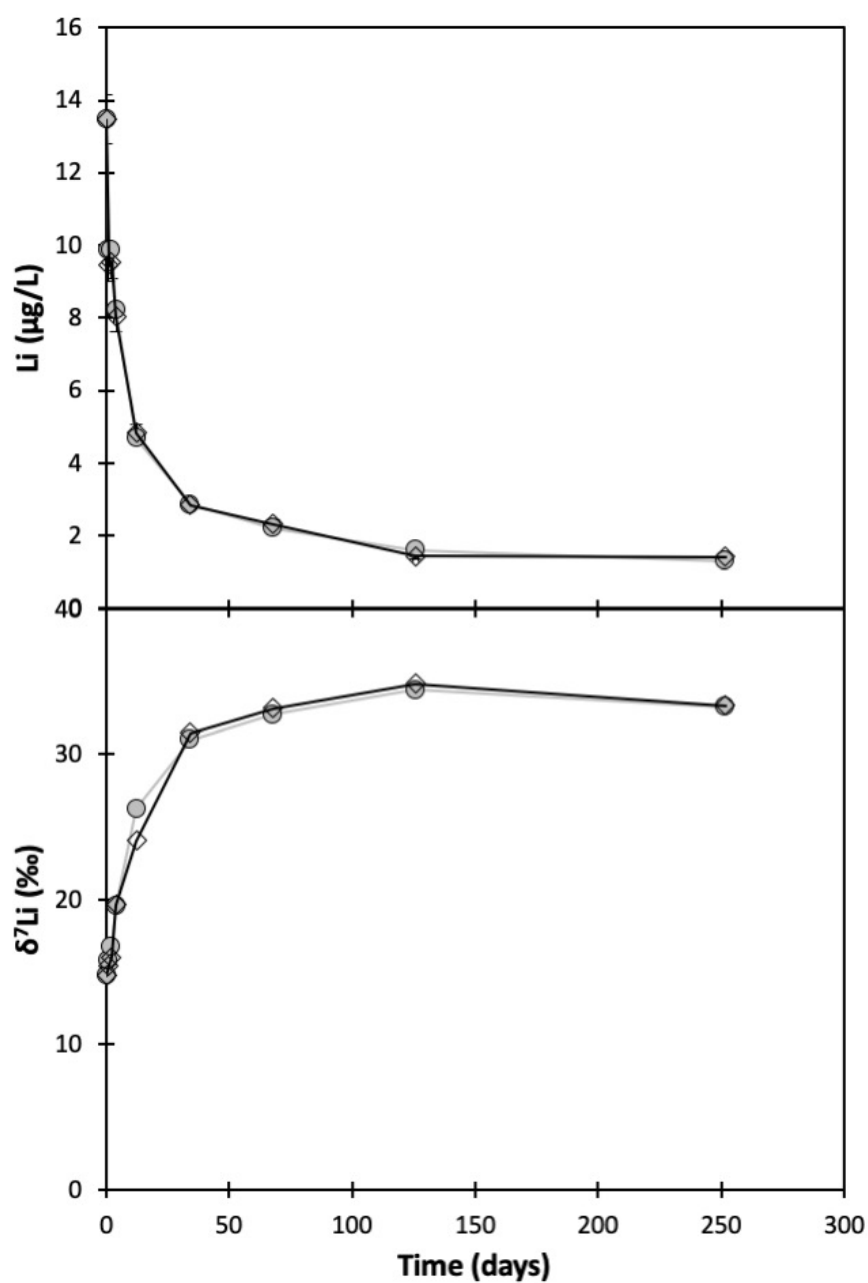


Figure 2. Solution Li concentrations and isotope ratios with time throughout the experiment. The open diamonds and filled circles represent the two different experiments. Analytical uncertainty is smaller than the symbol sizes.

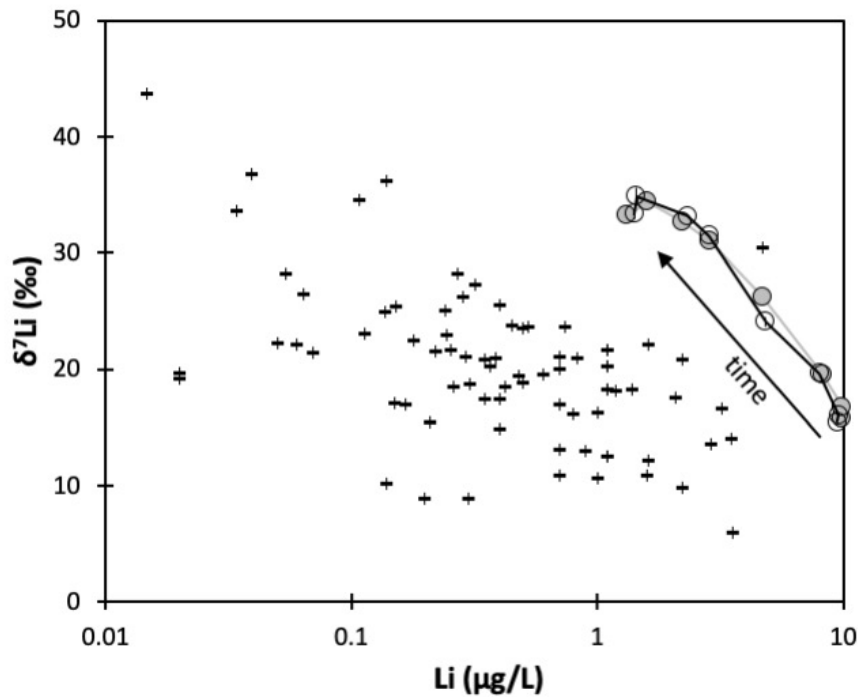


Figure 3. Measured Li isotopes ratios of the fluid phase from both experiments as a function of the corresponding Li concentration. The grey and black lines represent the two experiments. The black crosses are natural basaltic river studies (Liu et al., 2015; Pogge von Strandmann et al., 2010; Pogge von Strandmann et al., 2006; Vigier et al., 2009). Analytical uncertainty is smaller than the symbol sizes.

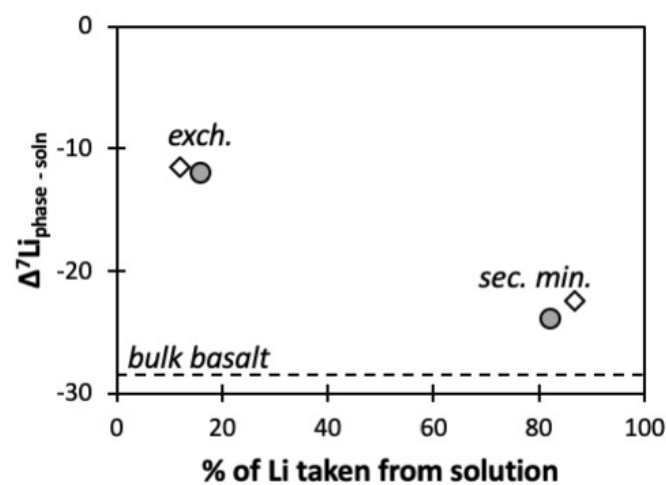


Figure 4. The mass balance of Li removed from solution by the different phases, relative to the isotope fractionation from the experimental solution. The filled circles represent Experiment 15, and the open diamonds Experiment 16.

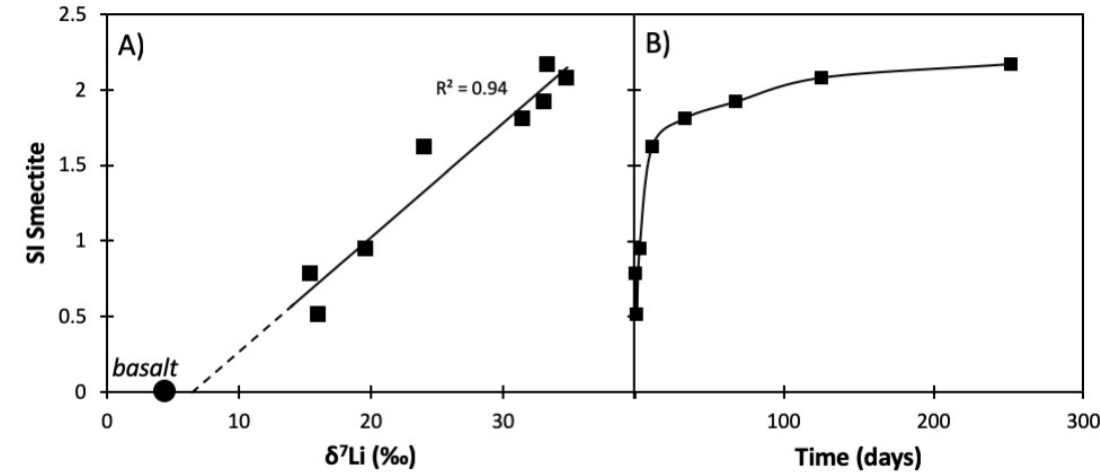


Figure 5. A) Li isotopes in solution as a function of PHREEQC-modelled smectite saturation index. The dotted line is the extrapolated trend line to saturated conditions. B) Trend of smectite saturation index with time during the experiment.

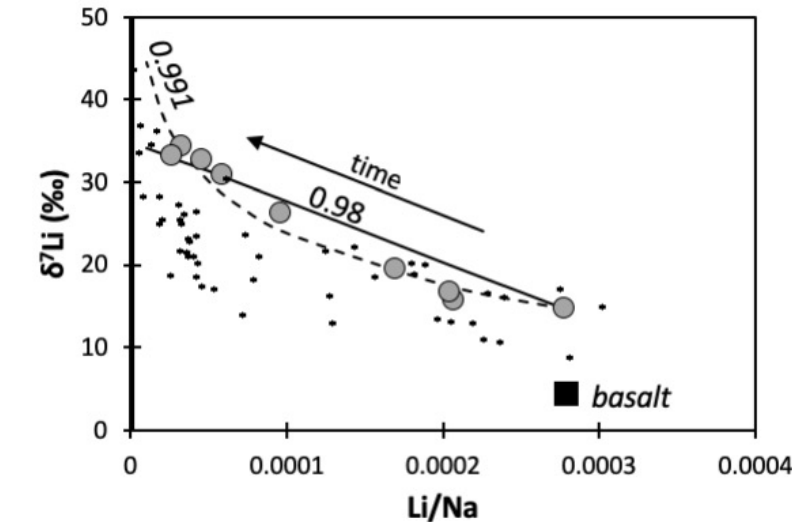


Figure 6. Experiment fluid $\delta^7\text{Li}$ as a function of corresponding mass Li/Na ratio (grey circles). The dotted illustrates a Rayleigh fractionation relationship, while the solid line represents an equilibrium fractionation relationship. The numbers

next to the lines are the isotopic fractionation factors. The black crosses are natural basaltic river studies (Liu et al., 2015; Pogge von Strandmann et al., 2010; Pogge von Strandmann et al., 2006; Vigier et al., 2009). Analytical uncertainty is smaller than the symbol sizes.

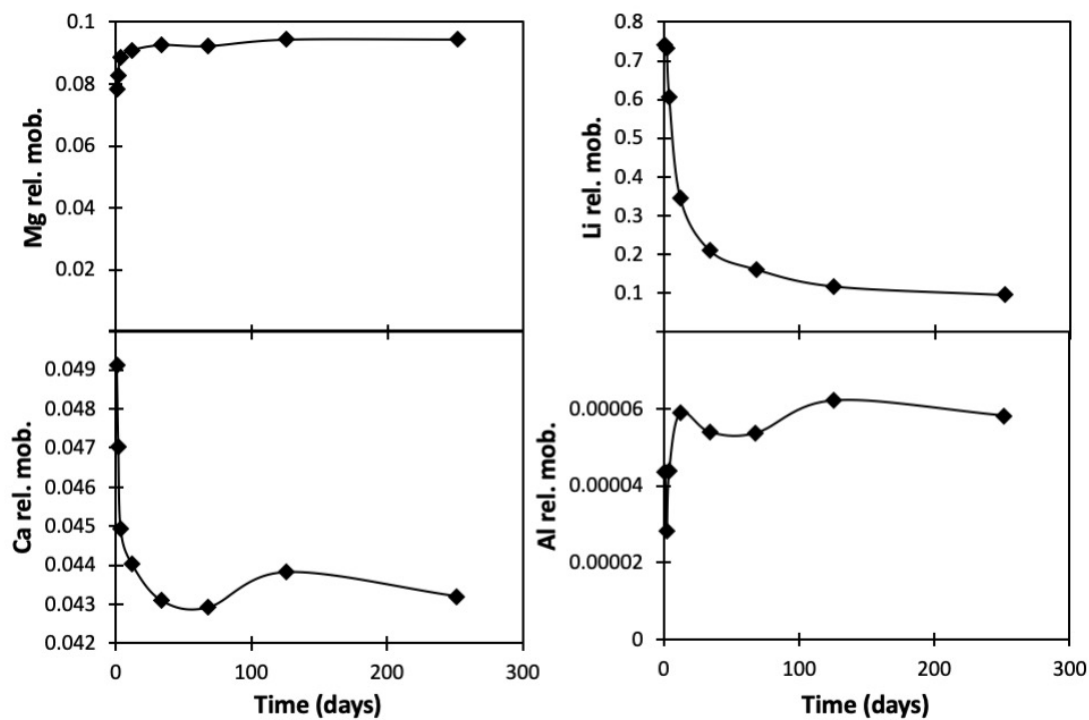


Figure 7. Relative mobility (relative to Na) of Mg, Li, Ca and Al with time through the experiment. Note different scale on axes.

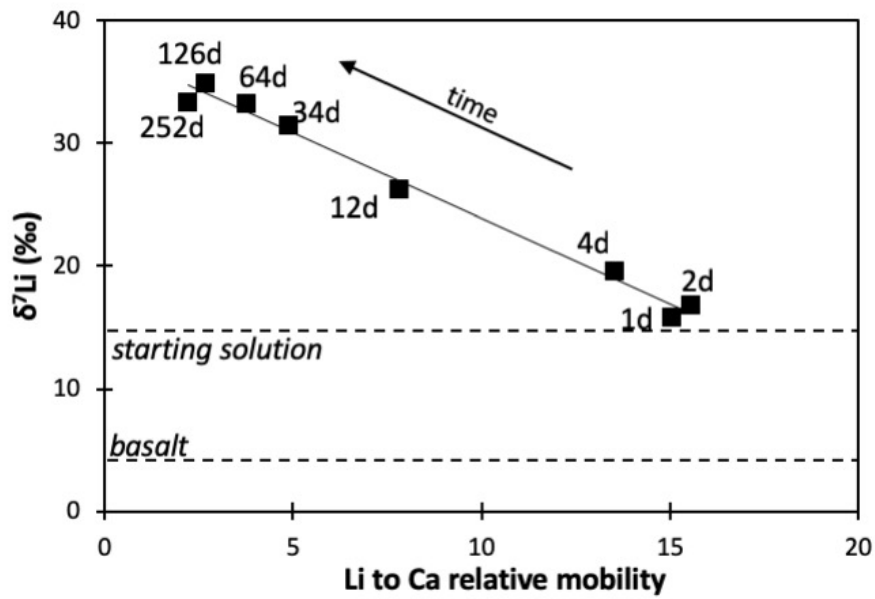


Figure 8. The reactive fluid Li isotopes ratio compared to the relative mobility of Li to Ca. The numbers next to each data point represent the experimental time (in days). Analytical uncertainty is smaller than the symbol sizes.